Distributions and Moments of Structural Properties for Percolation Clusters

Avidan U. Neumann[1] **and Shlomo Havlin**[1]

We study numerically and by scaling methods the distributions and moments of several structural properties of percolation clusters in two and three dimensions. The clusters are generated at criticality and properties such as the distribution of the mass as a function of linear size or chemical distance are studied. Our results suggest that the hierarchy of moments can be represented by a single gap exponent. Using a scaling approach, we obtain analytical forms for the different distribution functions which agree very well with the numerical data.

1. INTRODUCTION

The structural properties of percolation clusters have been a subject of considerable interest in recent years.[1-13] Several exponents have been found useful for characterizing the percolation cluster structure.[14,15] However, most of the effort has been expended on studying exponents that usually characterize first moment quantities. More information can be obtained from studying other moments and the entire information is included in the appropriate density distributions of which very little is known. For example, the concept of the fractal dimension[7] d_f of a random aggregate has attracted much interest in recent years. The fractal dimension of a random cluster characterizes the average mass M of the cluster within a radius R,

$$\langle M \rangle \approx R^{d_f} \tag{1.1}$$

Much effort has been devoted to studying this relation for different types of random aggregates.[16-22] Very little is known about the probability dis-

---

[1] Department of Physics, Bar-Ilan University, Ramat-Gan, Israel.

tribution $P(M|R)$, whose first moment is $\langle M \rangle$ in Eq. (1.1). Important concepts such as the lacunarity,[7,11] which characterizes the size distribution of "lakes" of empty sites, is related to the second moment $\langle M^2 \rangle$, and not much is known about it. The exponent for the second cumulant was studied also by Stauffer.[23]

Recently, probability distributions for several fractal properties such as the voltage distribution in percolation and the growth probabilities of diffusion-limited aggregation (DLA) have been found to be of *log-normal* type.[24-27] In these cases an infinite hierarchy of independent exponents (for which the term multifractal was coined) is needed to characterize the different moments.[28-30] Also, for the distribution of mass $P(M|R)$ in DLA, indications for multifractal behavior were found.[31] On the other hand, probability distributions such as $P(M|R)$ were studied analytically for percolation clusters generated on a Cayley tree and found to be of *normal* type.[32]

In the present work we study density distributions, moments, and cumulants of several structural properties of the incipient infinite percolation cluster embedded in two and three dimensions. We study the distribution of mass M within a radius $R - P(M|R)$ and within a chemical distance $l - P(M|l)$, and the distribution of R for a given chemical distance $l - P(R|l)$. We calculate numerically the moments and cumulants of the above quantities up to the 12th (and -12th) order. We find that the moments $\langle A^n \rangle$ scale as $\langle A \rangle^n$, indicating that the distributions are of normal type with a single gap exponent characterizing the infinite hierarchy of moments. Using a scaling approach, we suggest analytical forms for the different density distributions $P(M|R)$, $P(M|l)$, and $P(R|l)$. We find that $P(M|R)M$, $P(M|l)M$, and $P(R|l)R$ scale very well with the single parameter $x = M/R^{d_f}$, M/l^{d_l}, and $R/l^{\tilde{\nu}}$, respectively. Furthermore, the functional form of these functions for large x is found to be a "contracted" exponential, i.e., $\exp(-x^\delta)$ with $\delta > 1$.

2. METHOD

The distributions and the moments are calculated using various ensembles of site percolation clusters generated in two and three dimensions. The clusters are generated at criticality ($p = p_c = 0.5927$ in two dimensions and $p = p_c = 0.3117$ in three dimensions[4]) using the growth process presented by Leath[1] and Alexandrowicz.[5] In this method we start (at $t = 0$) with an occupied site taken as a seed at the origin of a hypercubic lattice. In the first step ($t = 1$) we mark its nearest neighbors as occupied or empty with probabilities p_c and $1 - p_c$, respectively. These occupied sites constitute a shell of chemical distance $l = 1$ from the origin.

At $t = 2$ the nearest neighbor sites (which were not tested earlier) of the first chemical shell are chosen to be occupied or empty with the same probabilities. The new occupied sites represent a chemical shell with $l = 2$. The process is repeated until no occupied sites exist in the new shell. If the cluster grows and "touches" the boundaries of the largest hypercubic box available by the computer memory, then the growth outward is stopped and is continued inside the box only.

The clusters were stored in the computer as a "bit hypermatrix", which was found useful for both time- and memory-saving. Although only a small part of the bit matrix is used, we find that for $D = 2$ and $D = 3$ it is still more efficient than using pointers,[6] which require much overhead in time and memory.

For each cluster we measure the following structural properties:

(a) $M(R)$, the mass (i.e., number of occupied sites) within a geometrical linear size R. We use the circular radius (i.e., distance from the center) as our linear size rather than a square box (i.e., distance from the axis). We checked and found that the difference between the circle and the square is only in the prefactors and not in the exponents, as expected.

(b) $M(l)$, the mass as a function of the number of chemical shells from the seed of the cluster (the number of chemical shells is also referred to in the literature as the chemical distance, topological distance, graph distance, or time.)

(c) $R(l)$, the geometrical distance of each site from an arbitrary given site as a function of its chemical distance.

(d) $l(R)$, the chemical distance of each site as a function of the geometrical distance.

For each of the above properties we calculate numerically the following quantities:

(i) *Average* or first moment,

$$\langle Y(x) \rangle = \sum_N Y(x)/N \tag{2.1}$$

where Y denotes M, R, or l; x denotes R or l; and N denotes the number of clusters for properties (a) and (b) and the number of sites for (c) and (d).

(ii) *Moments*,

$$\langle Y^n(x) \rangle = \sum_N Y^n(x)/N \tag{2.2}$$

where n is the order of the moment, $n = -12,..., -1, -0.5, -0.25, 0.25, 0.5, 1,..., 12$.

The moments in (2.2) are calculated using the distribution $F(Y|x)$ [see (iii)],

$$\langle Y^n(x) \rangle = \sum_Y Y^n F(Y|x) \Big/ \sum_Y F(Y|x) \tag{2.3}$$

From the various moments we calculate the *cumulants*,[33]

$$\langle \text{CUM}^n \rangle = \sum \{(-1)^{(i+1)}[n!/(i \cdot j!^i)]\langle Y^j \rangle^i\} \tag{2.4}$$

where the sum is over all the possible factorials (i, j) of n.

(iii)   *Distributions $F(Y|x)$*, the number of clusters or sites with a given x as a function of Y. In order to save memory space in the computer without losing accuracy, we used a "dynamical binning," i.e., for every x we divide differently the range of Y into small bins (ΔY); thus we obtain the maximum number of smallest bins. Using the distributions we calculate the *probability densities*,

$$P(Y|x) = F(Y|x) \Big/ \left[(\Delta Y) \cdot \sum_Y F(Y|x) \right] \tag{2.5}$$

Since we are interested in studying the properties of the incipient infinite cluster, we include in the statistics only those clusters that satisfy certain boundary conditions (B.C.). We use several types of B.C., and for each of them we generate an ensemble of clusters:

(a)   The clusters are grown until a certain (large) chemical shell l is reached and then the process is stopped (this will be referred to as *fixed l*). Those clusters that do not reach the number of shells l are excluded from the ensemble.

(b)   The clusters are grown until they "die" and only those that reach at least a minimum shell l are included (*min l*).

(c)   Only clusters that reach all $2D$ boundaries of the largest box available, which is of size $(2R)^D$, are included (*fixed R*). In this case they grow only inside the box.

(d)   The clusters are grown until they "die" and only those that reach at least all $2D$ boundaries of a box of size $(2R)^D$ are included (*min R*). In this case they also grow outside the box.

It is important to mention that all ensembles of B.C. (a) and (c) are disjoint to each other, while ensembles generated using B.C. (b) and (d) may be contained in one another if they were grown on the same lattice, since they have the same pseudorandom seed.

Each of the above B.C. has some boundary effects on the properties measured and one has to take these into consideration in order to get the less biased ensemble of clusters. For example, when using fixed R there exist boundary effects for large values of l. This is because only very dense clusters can reach all $2D$ boundaries from inside, and thus the shells near the boundaries are "over massed." There also exist boundary effects for the case of fixed l. This B.C. is not useful when measuring $M(R)$, since many sites within a certain R will be occupied only by larger shells.

We used for the simulations an IBM-3090 (7000 Kb memory). The average time for growing a 200-shell cluster in $D = 2$ is 2.25 sec, and for 1000 shells is 23 sec. In $D = 2$ we tested altogether 7.8×10^9 sites in 375 hr, which results in 5800 sites/sec, and in $D = 3$, 2.3×10^9 sites in 187.5 hr, which gives about 3500 sites/sec.

In $D = 2$ we generated 10,000 clusters for each of the eight disjoint ensembles with cluster sizes 400×400 and the B.C.: fixed $l = 300$, fixed $R = 200$, and six smaller values, and about 3000 clusters of cluster size 2000×2000 for each of the B.C. min $l = 300$, 1000, 2000, 3000, and 4000 and min $R = 200$, 600, and 1000.

In $D = 3$ we generated 10,000 clusters of size $100 \times 100 \times 100$ for each of the B.C. min $l = 200$, 500, and 800 and min $R = 10$, 20, 30, 40, and 50.

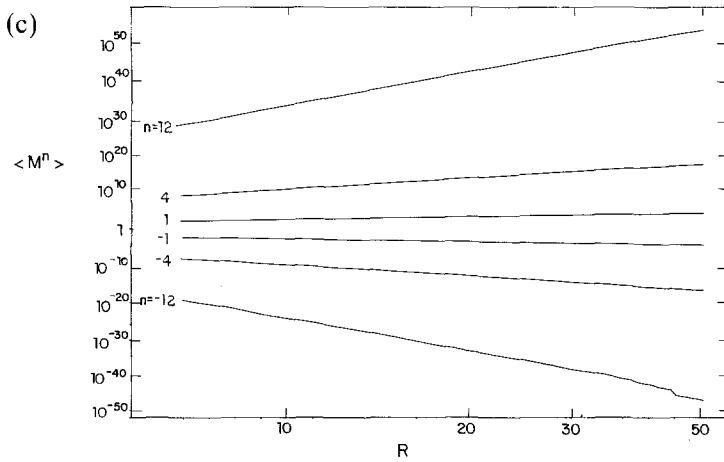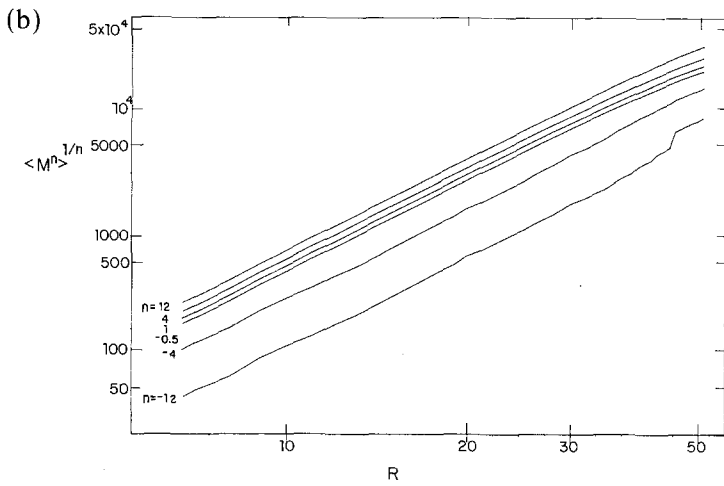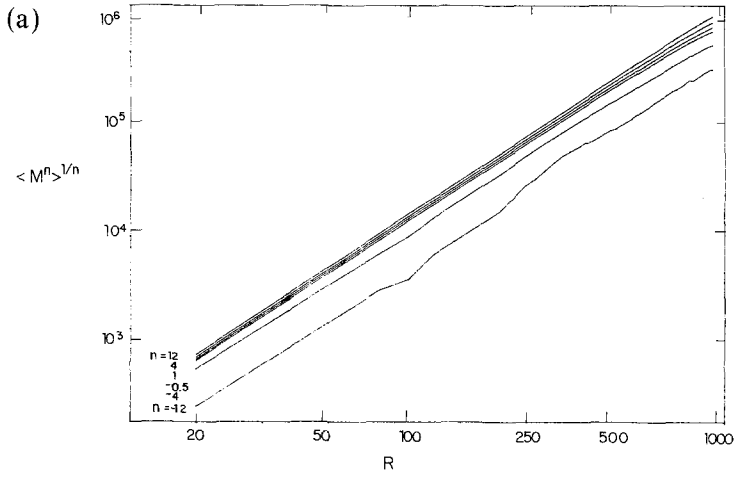## 3. RESULTS: MOMENTS AND CUMULANTS

3.1. $M(R)$

We begin by presenting our numerical results for the moments $\langle M^n \rangle$ as a function of R in two and three dimensions (see Fig. 1). We expect the first moment, i.e., the average of the mass, to scale as

$$\langle M \rangle = A R^{d_f} \tag{3.1}$$

where A is a constant and d_f is the fractal dimension of the perculation cluster. Indeed, the plot of $\log \langle M \rangle$ versus $\log R$ gives a straight line with a slope equal to the fractal dimension. In $D = 2$ the best fit gives $d_f = 1.90 \pm 0.01$, which is very close to the value given by theory, $d_f = 91/48$,[4] and in $D = 3$ we get $d_f = 2.50 \pm 0.02$, in aggrement with previous results.[4,8] Note that very similar values of d_f are obtained by a scaling approach (see Section 4).

In Figs. 1a and 1b we plot $\log(\langle M^n \rangle^{1/n})$ versus $\log R$ for values of n in the range $-12 \leqslant n \leqslant 12$. It is seen that all lines have the same slope, indicating that all moments follow the form

$$\langle M^n \rangle = A_n R^{d_n}, \qquad d_n = n d_f \tag{3.2}$$

(a)

$\langle M^n \rangle^{1/n}$

10^6

10^5

10^4

10^3

n = 12
4
1
-0.5
-4
n = -12

20   50   100   250   500   1000

R

(b)

$\langle M^n \rangle^{1/n}$

5×10^4

10^4

5000

1000

500

100

50

n = 12
4
1
-0.5
-4

n = -12

10   20   30   50

R

(c)

$\langle M^n \rangle$

10^{50}
10^{40}
10^{30}
10^{20}
10^{10}
1
10^{-10}
10^{-20}
10^{-30}
10^{-40}
10^{-50}
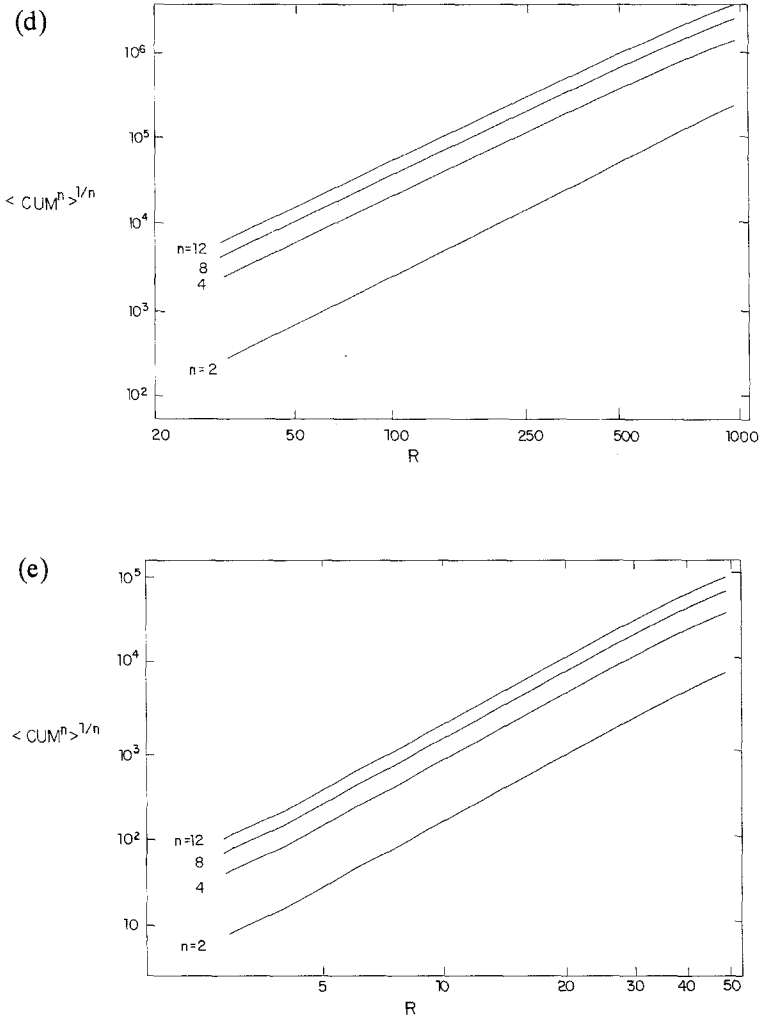
n = 12

4

1

-1

-4

n = -12

10   20   30   50

R

Fig. 1. Various plots of the moments of $M(R)$. (a, b) Plot of $\log(\langle M^n \rangle^{1/n})$ versus $\log R$ with B.C. min $l = 4000$ for $D = 2$ and min $l = 500$ for $D = 3$, respectively. All the lines have the same slope, except for slight deviations at the boundaries (best fit results are given in Table I). (c) Plot of $\log\langle M^n \rangle$ versus $\log R$ for $D = 3$ (min $l = 500$). Negative and positive moments are almost symmetrical. (d, e) Plot of $\log(\langle CUM^n \rangle^{1/n})$ (of mass) versus $\log R$ for $D = 2$ (min $l = 4000$) and $D = 3$ (min $l = 500$), respectively. All lines have the same slope, except for large R, due to boundary effects. Best fit results are presented in Table I.

and a single gap exponent d_f characterizes all moments. The values of A_n and d_n obtained from a best fit of Eq. (3.2) to the data are given in Table I. In Fig. 1c we plot $\log \langle M^n \rangle$ versus $\log R$, showing that positive and negative moments are almost symmetrical; the differences being only in the prefactors A_n.

We also calculate the ratios $\langle M^n \rangle / \langle M \rangle^n$ versus R, which are expected to be constants equal to A_n / A_1^n. However, we find that boundary effects are very strong and make this difficult to see. Nevertheless, the larger the clusters are taken, the better is the constant line seen, indicating that $\langle M^n \rangle / \langle M \rangle^n$ approaches a constant for large R.

We calculate several cumulants, which are important since they provide more information about the form of the distribution function. The cumulants are assumed to follow the scaling form

$$\langle \mathrm{CUM}^n \rangle = C_n R^{d'_n}, \qquad d'_n = d_n = n d_f \qquad (3.3)$$

since they are only the differences between the appropriate moments. Indeed, as seen in Figs. 1d and 1e, here also one gets parallel straight lines when ploting $\log \langle \mathrm{CUM}^n \rangle$ versus $\log R$, suggesting that a single gap exponent characterizes all the cumulants. The values of C_n are given in Table I. The second cumulant is of special interest because of its relation to the *lacunarity*,[7,11] which is defined by its prefactor C_2.

Table I. Numerical Estimates of A_n and d_n for Several Moments of $M(R)$ ($\langle M^n \rangle = A_n R^{d_n}$) and C_n for the Cumulants of the Mass ($\langle \mathrm{CUM}^n \rangle = C_n R^{d_n}$)

	$D = 2$			$D = 3$		
n	$\log A_n$	d_n	$\log C_n$	$\log A_n$	d_n	$\log C_n$
-12	5.0 ± 0.3	-23.1 ± 0.5	—	25.3 ± 0.9	-34.1 ± 0.5	—
-8	0.7 ± 0.2	-15.07 ± 0.1	—	13.5 ± 0.6	-22.2 ± 0.1	—
-4	-3.0 ± 0.1	-7.65 ± 0.05	—	2.2 ± 0.4	-11.6 ± 0.05	—
-2	-2.1 ± 0.1	-3.85 ± 0.02	—	0.23 ± 0.10	-4.99 ± 0.03	—
-1	-1.0 ± 0.1	-1.92 ± 0.02	—	-0.13 ± 0.05	-2.59 ± 0.03	—
-0.5	0.52 ± 0.05	-0.95 ± 0.01	—	-0.09 ± 0.05	-1.28 ± 0.01	—
0.5	0.55 ± 0.05	0.95 ± 0.01	—	0.15 ± 0.05	1.26 ± 0.01	—
1	0.8 ± 0.1	1.90 ± 0.01	—	0.4 ± 0.1	2.50 ± 0.01	—
2	1.6 ± 0.1	3.81 ± 0.01	-1.1 ± 0.2	0.85 ± 0.1	5.03 ± 0.01	-0.40 ± 0.1
4	3.2 ± 0.1	7.61 ± 0.01	4.4 ± 0.3	2.2 ± 0.1	10.09 ± 0.03	3.8 ± 0.2
8	6.3 ± 0.2	15.15 ± 0.02	13.3 ± 0.3	4.4 ± 0.2	20.10 ± 0.05	12.0 ± 0.5
12	9.7 ± 0.2	22.76 ± 0.02	24.5 ± 0.4	8.7 ± 0.3	30.3 ± 0.1	22.5 ± 0.7

3.2. $M(l)$

Next we present the moments $\langle M^n \rangle$ as a function of l in two and three dimensions (see Fig. 2). We expect the first moment, i.e., the average of the mass, to scale as

$$\langle M \rangle = Al^{d_l} \qquad (3.4)$$

where A is a constant and d_l is a topological fractal dimension. Indeed, the plot of $\log\langle M \rangle$ versus $\log l$ gives a straight line and the slope gives results for d_l close to previous results.[5,8,9] In $D = 2$ the best fit gives $d_l = 1.66 \pm 0.01$, and in $D = 3$ we get $d_l = 1.75 \pm 0.01$. Very similar values of d_l are also obtained by using a scaling approach (see Section 4).

In Figs. 2a and 2b we plot $\log(\langle M^n \rangle^{1/n})$ versus $\log l$ for values of n in the range $-12 \leqslant n \leqslant 12$. All lines have the same slope, indicating that all moments follow the form

$$\langle M^n \rangle = A_n l^{d_n}, \qquad d_n = nd_l \qquad (3.5)$$

and a single gap exponent d_l characterizes all moments.

In Fig. 2c we plot $\log\langle M^n \rangle$ versus $\log l$, showing that positive and negative moments are almost symmetrical.

We calculate several cumulants for $M(l)$, which are assumed to follow the scaling form

$$\langle \mathrm{CUM}^n \rangle = C_n l^{d'_n}, \qquad d'_n = d_n = nd_l \qquad (3.6)$$
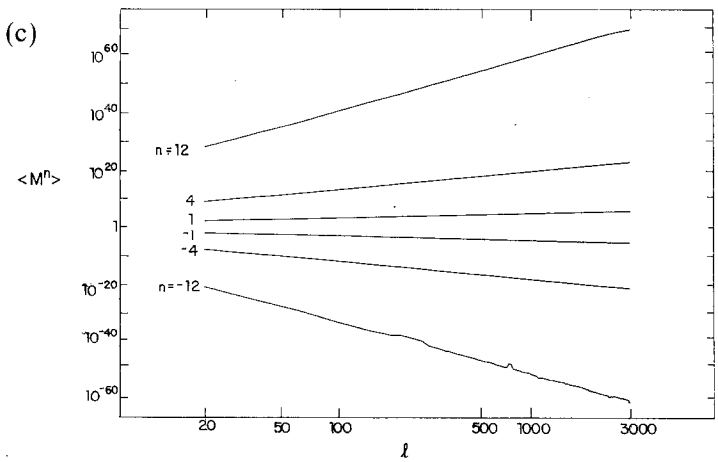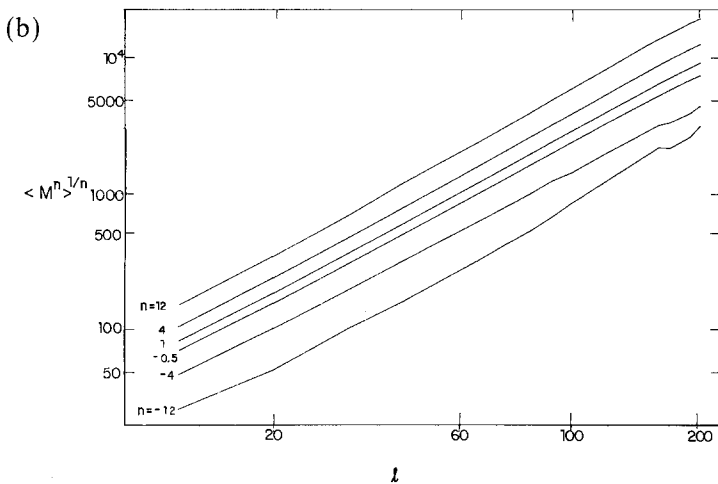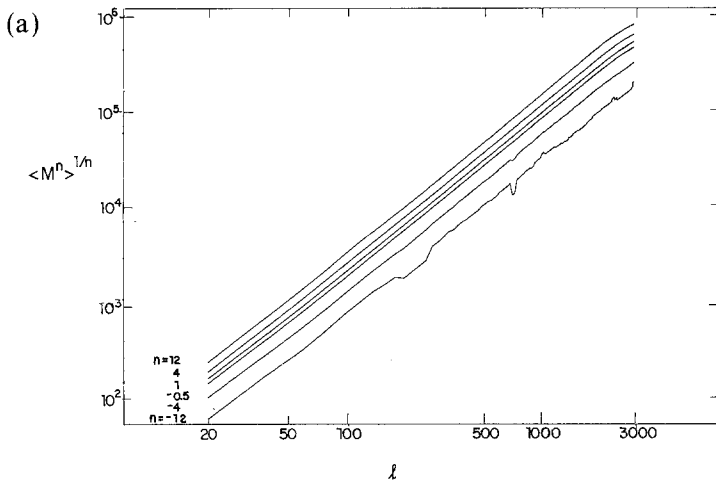
As seen in Figs. 2d and 2e, here also parallel straight lines are obtained when ploting $\log\langle \mathrm{CUM}^n \rangle$ versus $\log l$, suggesting that a single gap exponent characterizes all the cumulants of $M(l)$.

3.3. $R(l)$

The first moment of the geometrical distance $\langle R \rangle$ between any two sites on the incipient infinite percolation cluster as a function of the chemical distance l is given by[9]

$$\langle R \rangle = Al^{\tilde{\nu}} \qquad (3.7)$$

where $\tilde{\nu}$ is an exponent that relates the extrinsic distance R to the intrinsic distance l. The value of $\tilde{\nu}$ is obtained using two methods. The first is by applying a best fit of Eq. (3.7) to the numerical data presented in Fig. 3.

(a)

$\langle M^n \rangle^{1/n}$

n=12
4
1
-0.5
-4
n=-12

ℓ

(b)

$\langle M^n \rangle^{1/n}$

n=12
4
1
-0.5
-4

n=-12

ℓ

(c)

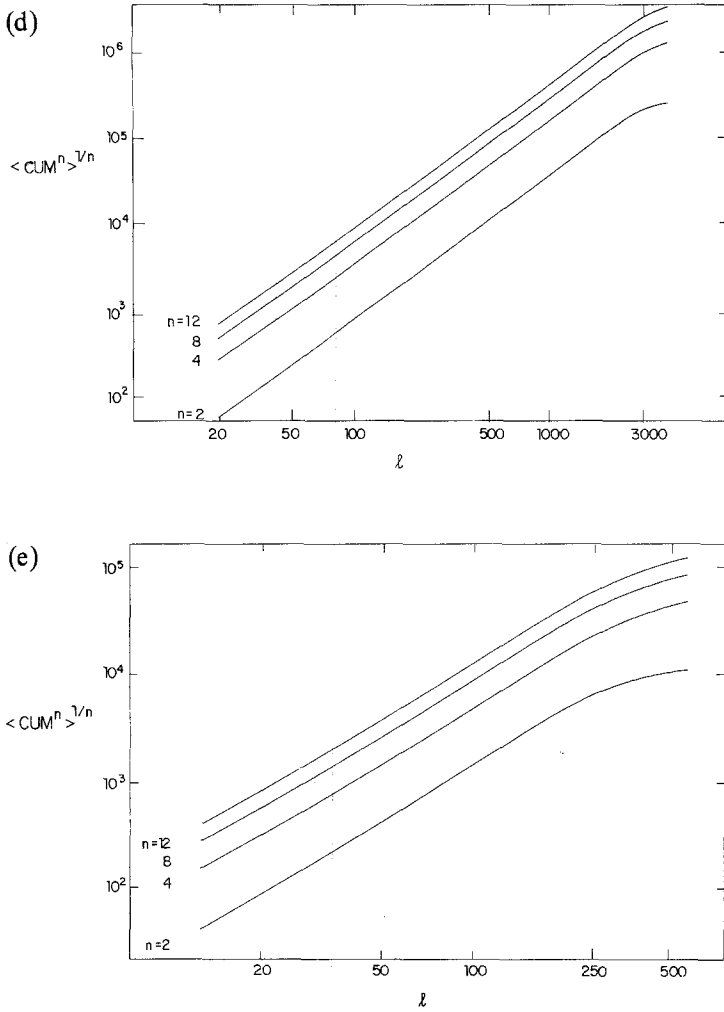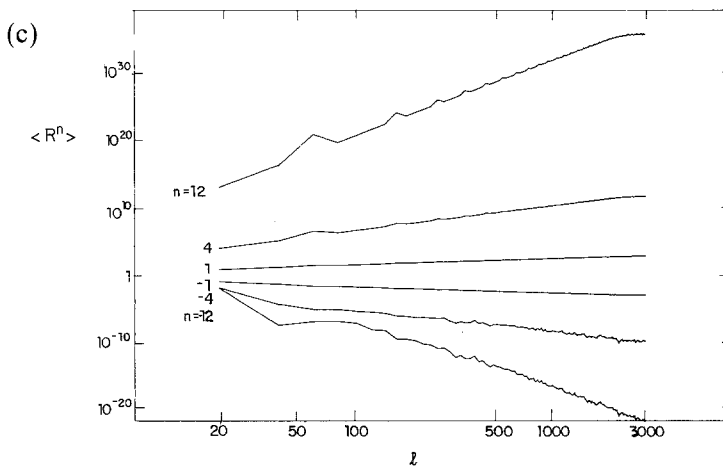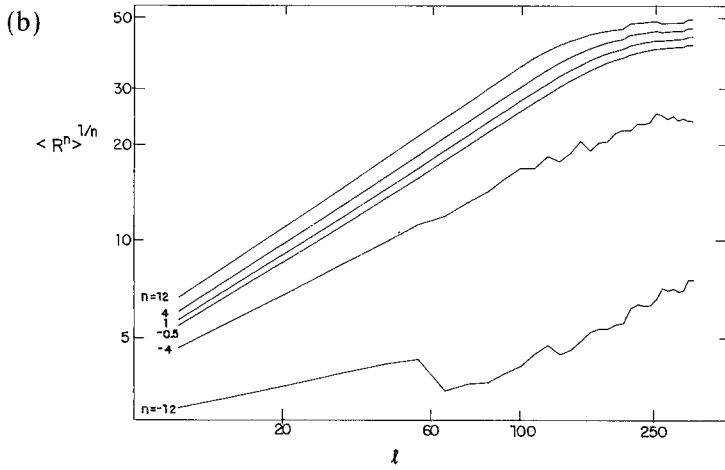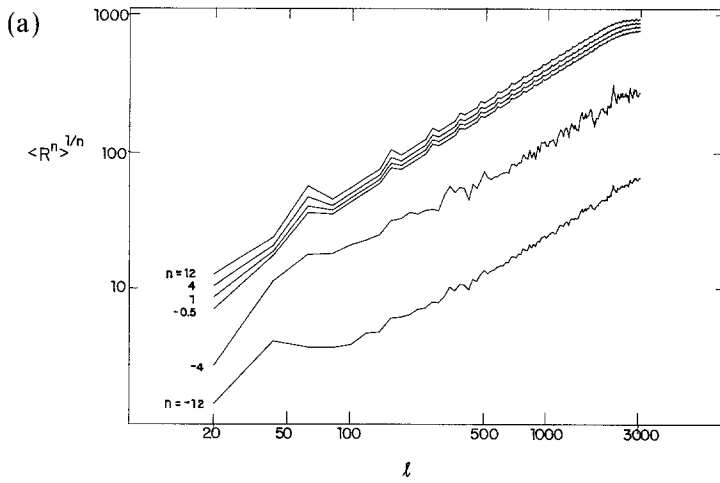$\langle M^n \rangle$

n=12

4
1
-1
-4

n=-12

ℓ

Fig. 2. Various plots of moments of $M(l)$. (a, b) Plot of $\log(\langle M^n \rangle^{1/n})$ versus $\log l$ for $D = 2$ (B.C. min $l = 3000$) and $D = 3$ (min $l = 200$), respectively. All lines have the same slope, except at the boundaries. (c) Plot of $\log\langle M^n \rangle$ versus $\log l$ for $D = 2$ (min $l = 3000$). Negative and positive moments are almost symmetrical. (d, e) Plot of $\log(\langle \mathrm{CUM}^n \rangle^{1/n})$ (of mass) versus $\log l$ for $D = 2$ (min $l = 4000$) and $D = 3$ (min $l = 500$), respectively. All lines have the same slope, except at the boundaries.
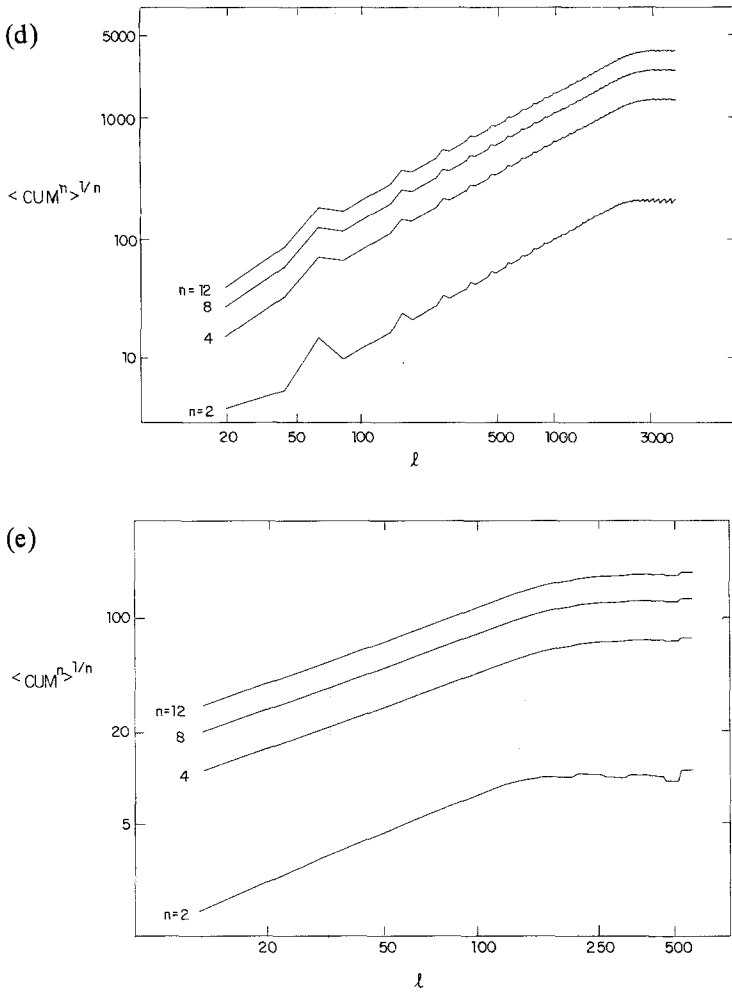
(a)

$\langle R^n \rangle^{1/n}$

1000

100

10

n = 12
4
1
-0.5

-4

n = -12

20   50   100   500   1000   3000

ℓ

(b)

$\langle R^n \rangle^{1/n}$

50

30

20

10

5

n=12
4
1
-0.5
-4

n=-12

20   60   100   250

ℓ

(c)

$\langle R^n \rangle$

10^{30}

10^{20}

10^{10}

1

10^{-10}

10^{-20}

n =12

4

1

-1
-4
n=12

20   50   100   500   1000   3000

ℓ

Fig. 3. Various plots of moments of $R(l)$. (a, b) Plot of $\log(\langle R^n \rangle^{1/n})$ versus $\log l$ for $D = 2$ (B.C. min $l = 3000$) and $D = 3$ (min $R = 40$), respectively. All the positive moments have the same slope, except at the boundaries. The negative moments show a drop in the slope for small l, but the slope is the same as for the positive moments for large l. Best fit results are given in Table II. (c) Plot of $\log\langle R^n \rangle$ versus $\log l$ for $D = 2$ (min $l = 3000$). It is seen that negative moments are asymmetrical to positive moments. (d, e) Plot of $\log(\langle \text{CUM}^n \rangle^{1/n})$ (of radius) versus $\log l$ for $D = 2$ (min $l = 4000$) and $D = 3$ (min $l = 500$), respectively. All the lines have the same slope except at the boundaries. Best fit results are given in Table II.
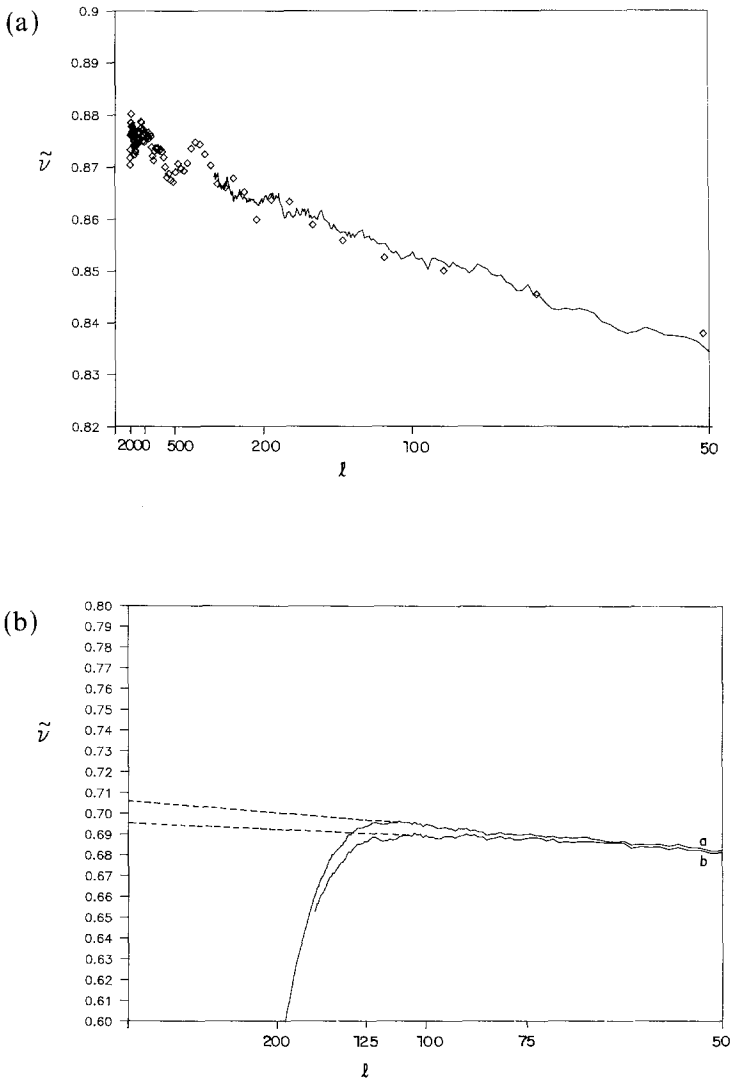
Fig. 4. The exponent $\tilde{\nu}$ as calculated by an extrapolation method.[8] (a) Results for $D = 2$. The solid line is for min $l = 300$ and the points are for min $l = 2000$. The extrapolation of the lines gives $\tilde{\nu} = 0.875 \pm 0.005$. (b) Results for $D = 3$. Line a is for min $l = 200$ and line b is for min $R = 20$. The extrapolation of the lines gives $\tilde{\nu} = 0.700 \pm 0.005$. The drop of the lines for large l is due to boundary effects.

A second and more accurate method uses an extrapolation method similar to that applied by Grassberger.[8] Calculating the quantity

$$E(l) = l\langle R(l)\rangle \bigg/ \left[0.5\langle R(l)\rangle + \sum_{l'=1,l-1} \langle R(l')\rangle \right] \qquad (3.8)$$

one can see that

$$E(l) = l^{\tilde{v}+1}/[0.5l^{\tilde{v}} + (\tilde{v}+1)^{-1}(l-1)^{\tilde{v}+1}]$$

and thus

$$\lim_{l\to\infty} E(l) = \tilde{v}+1$$

By plotting $E(l) - 1$ versus $1/l$ one can extrapolate $\tilde{v}$. This method yields $\tilde{v} = 0.875 \pm 0.005$ for $D = 2$ and $\tilde{v} = 0.70 \pm 0.01$ for $D = 3$ (Fig. 4). Note that these results are slightly lower than the previous estimates[8] $\tilde{v} = 0.883 \pm 0.003$ for $D = 2$ and $\tilde{v} = 0.725 \pm 0.006$ for $D = 3$. These numerical deviations may result from the different growth methods of the infinite cluster used in these studies. While in the present work the clusters were generated from a single site seed, in ref. 8 a hyperplane of dimension $D - 1$ was used as a seed.

Higher moments of $\langle R^n\rangle$ are also shown in Fig. 3. It is seen from Figs. 3a and 3b that for large l all curves of $\log(\langle R^n\rangle^{1/n})$ as a function of $\log l$ yield parallel straight lines. This is consistent with the following form for the moments:

$$\langle R^n\rangle = A_n l^{\tilde{v}_n} \qquad (3.9)$$

The values of A_n and $\tilde{v}_n$ obtained by best fit to the data are presented in Table II, confirming that $\tilde{v}_n = n\tilde{v}$ and a single gap-exponent characterizes all the moments $\langle R^n\rangle$.

For small l, one can see from Fig. 3 that the slopes of the negative moments decrease as n decreases. This can be seen better in Fig. 3c, where $\langle R^n\rangle$ is plotted versus l. This behavior may be attributed to the discreteness of the lattice and due to the fact that negative moments of $\langle R_n\rangle$ are dominated by small values of R. The smaller the value of l, the smaller are the values of R that are relevant, and these are strongly affected by the discreteness of the lattice.

In Figs 3d and 3e the corresponding cumulants of the above moments are shown.

Table II.   Numerical Estimates of A_n and d_n for Several Moments of $R(l)$
$(\langle R^n \rangle = A_n l^{\tilde{v}_n})$ and C_n for the Cumulants of the Radius $(\langle CUM^n \rangle = C_n l^{\tilde{v}_n})$

|	$D = 2$			$D = 3$		
n	$\log A_n$	$\tilde{v}_n$	$\log C_n$	$\log A_n$	$\tilde{v}_n$	$\log C_n$
−12	37.0 ± 0.2	10.6 ± 0.2	—	15.3 ± 0.2	-7.9 ± 0.5	—
−8	20.7 ± 0.1	7.1 ± 0.1	—	3.0 ± 0.1	-4.9 ± 0.3	—
−4	5.15 ± 0.05	-3.50 ± 0.05	—	1.70 ± 0.03	-2.9 ± 0.2	—
−2	0.74 ± 0.02	-1.75 ± 0.02	—	0.28 ± 0.02	-1.3 ± 0.1	—
−1	0.27 ± 0.02	-0.88 ± 0.01	—	-0.13 ± 0.01	-0.7 ± 0.06	—
−0.5	0.11 ± 0.01	-0.44 ± 0.01	—	-0.07 ± 0.01	-0.34 ± 0.04	—
0.5	0.09 ± 0.01	0.44 ± 0.01	—	0.07 ± 0.01	0.35 ± 0.02	—
1	-0.19 ± 0.01	0.88 ± 0.01	—	0.13 ± 0.01	0.68 ± 0.02	—
2	-0.32 ± 0.01	1.76 ± 0.01	-3.20 ± 0.05	0.28 ± 0.01	1.39 ± 0.02	-3.1 ± 0.1
4	-0.46 ± 0.02	3.53 ± 0.01	1.33 ± 0.03	0.64 ± 0.02	2.82 ± 0.02	2.6 ± 0.1
8	-0.46 ± 0.02	7.07 ± 0.02	7.13 ± 0.05	1.50 ± 0.05	5.70 ± 0.05	9.7 ± 0.1
12	-0.26 ± 0.03	10.61 ± 0.05	15.2 ± 0.08	$2.6 + 0.1$	8.5 ± 0.1	19.1 ± 0.3
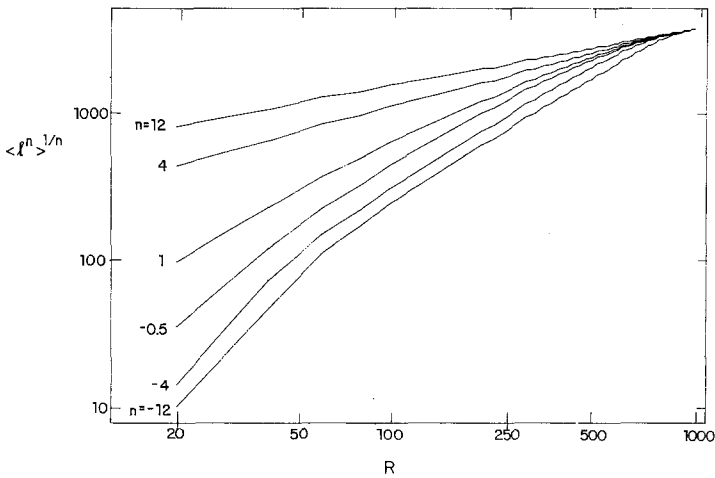
Fig. 5.   Plot of $\log(\langle l^n \rangle^{1/n})$ versus $\log R$ for $D = 2$ (B.C. min $l = 3000$). For the positive moments the lines are not parallel, but for the negative moments they become more parallel as n is decreased.

3.4. $l(R)$

When calculating $\langle l \rangle$ for a given R, strong boundary effects are noticed. This is due to the fact that for a given R, occupied sites with large l are missing in the statistics. For the positive moments $\langle l^n \rangle$, $n > 0$, sites with large l are the dominant ones and since they are missing, the plot of $\log \langle l^n \rangle$ is not linear with $\log R$. On the other hand, the negative moments are dominated by sites with small l and therefore are less influenced by boundary effects, as can be seen in Fig. 5. In any case, our method of growing the percolation clusters is not efficient for measuring $l(R)$.

4. RESULTS: DISTRIBUTIONS AND SCALING

4.1. $P(M|R)$

We begin our study of the distributions by ploting the numerical data for $\log P(M|R)$ as a function of $\log M$ for various values of R (see Fig. 6a). This figure presents the general form of the probability for having a mass M within a given radius R.

To test whether the probability distribution $P(M|R)$ can be presented in a scaling form, we plot $P(M|R)/P(M|R)_{\max}$ (i.e., we normalize every probability by the highest probability value in the same R) as function of $M/M_{1/2}$ (i.e., each mass is normalized by the value of one-half of the largest mass in the same R); see Fig. 6b. It is seen that the different curves in Fig. 6a collapse to a single curve in Fig. 6b, indicating the scaling property of $P(M|R)$.

In the above normalization scaling method we did not impose any assumption on the form of $P(M|R)$. Indeed, a simple scaling assumption that yields the above scaling properties as well as the results for the moments found in Eqs. (3.1)–(3.3) is
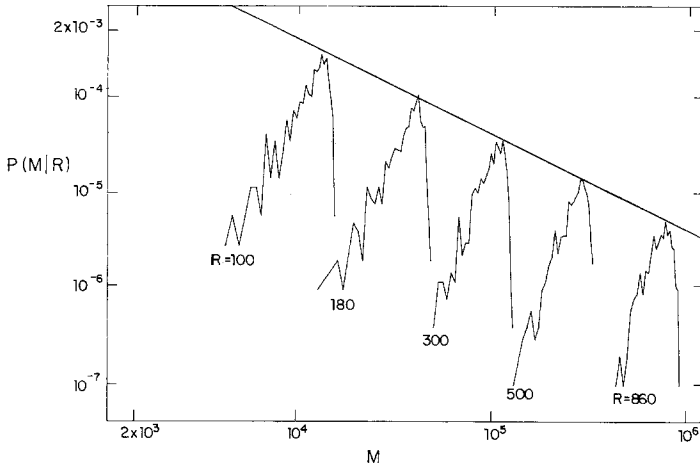
$$P(M|R) \approx M^{-1} f_1(M/R^{d_f}) \tag{4.1}$$
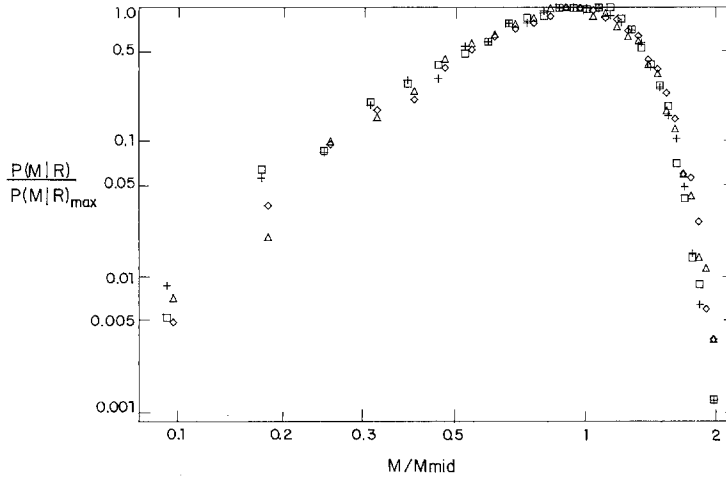
which is the simplest form that yields the relation

$$\langle M \rangle = \int MP(M|R)\,dM \approx R^{d_f} \tag{4.2}$$

The factor M^{-1} in Eq. (4.1) comes from the normalization condition,

$$\int P(M|R)\,dM = 1 \tag{4.3}$$

(a)

(b)

Fig. 6. (a) Plot of $\log P(M \mid R)$ versus $\log M$ for several values of R for $D = 2$ (B.C. fix $R = 1000$). The straight line connecting the maxima of these plots has a slope of -1. (b) Plot of $\log\{P(M \mid R)/P(M \mid R)_{\max}\}$ versus $\log\{M/M_{1/2}\}$ for $D = 3$ (B.C. min $l = 500$) for several values of R: ($\square$) 20, ($+$) 25, ($\Diamond$) 30, and ($\triangle$) 35.

Other moments can be calculated using Eq. (4.1),

$$\langle M^n \rangle = \int M^n M^{-1} f_1(M/R^{d_f}) \, dM \approx R^{nd_f} \tag{4.4}$$

where d_f is the gap exponent characterizing all the moments. The scaling form of Eq. (4.1) is also supported by the straight line connecting the maximas $P(M^*|R)$ in Fig. 6a, which has a slope -1. By taking the logarithm of both sides of Eq. (4.1),

$$\log P(M|R) = -\log M - \log f_1(M/R^{d_f}) \tag{4.5}$$

and assuming the scaling property that $f_1(M/R^{d_f})$ is a constant for $M = M^*$, one obtains a slope of -1, as seen in Fig. 6a.

To test directly the scaling form suggested in Eq. (4.1), we plot in Figs. 7a and 7d $P(M|R)M$ as a function of M/R^{d_f}. The data collapse shows excellent agreement with the above scalling form. The best scaling is obtained using $d_f = 1.896 \pm 0.002$ for $D = 2$ and $d_f = 2.50 \pm 0.02$ for $D = 3$. This method of scaling provides an accurate method for determining d_f, as it is very sensitive to the chosen value of d_f.

In Figs. 7b and 7e we plot $\log(P(M|R)M)$ as a function of $\log M$ for $D = 2$ and $D = 3$, respectively. For $M < M^*$ [M^* is the mass that has maximum probability $P(M|R)$], the data points form a line that is nearly straight. This indicates that $f_1(x)$ is governed by a power law in this regime. Above M^*, $f_1(x)$ falls sharply, suggesting that an exponential form governs this regime. Thus, we assume that $f_1(x)$ has a *power-exp* form,

$$f_1(x) = A_1 x^{g_1} \exp(-B_1 x^{\delta_1}), \qquad x = M/R^{d_f} \tag{4.6}$$

Using best fit techniques for fitting the data to Eq. (4.6), we obtain numerical values for A_1, B_1, g_1, and δ_1 given in Table III.

Table III. The Parameters Obtained from a Best Fit to the Scaling form of $P(M|R)$[a]

	$D = 2$	$D = 3$
d_f	1.896 ± 0.002	2.50 ± 0.02
A_1	0.020 ± 0.004	0.06 ± 0.01
g_1	6.9 ± 0.1^a, 0.0047 ± 0.0005^b	6.3 ± 0.2
B_1	$7.0 \times 10^{-8} \pm 1.0 \times 10^{-8}$	0.055 ± 0.010
δ_1	19.1 ± 0.1^a, 19.2 ± 0.2^b	4.2 ± 0.1

[a] Eq. (4.6), $f_1(X) = A_1 X^{g_1} \exp(-B_1 X^{\delta_1})$.
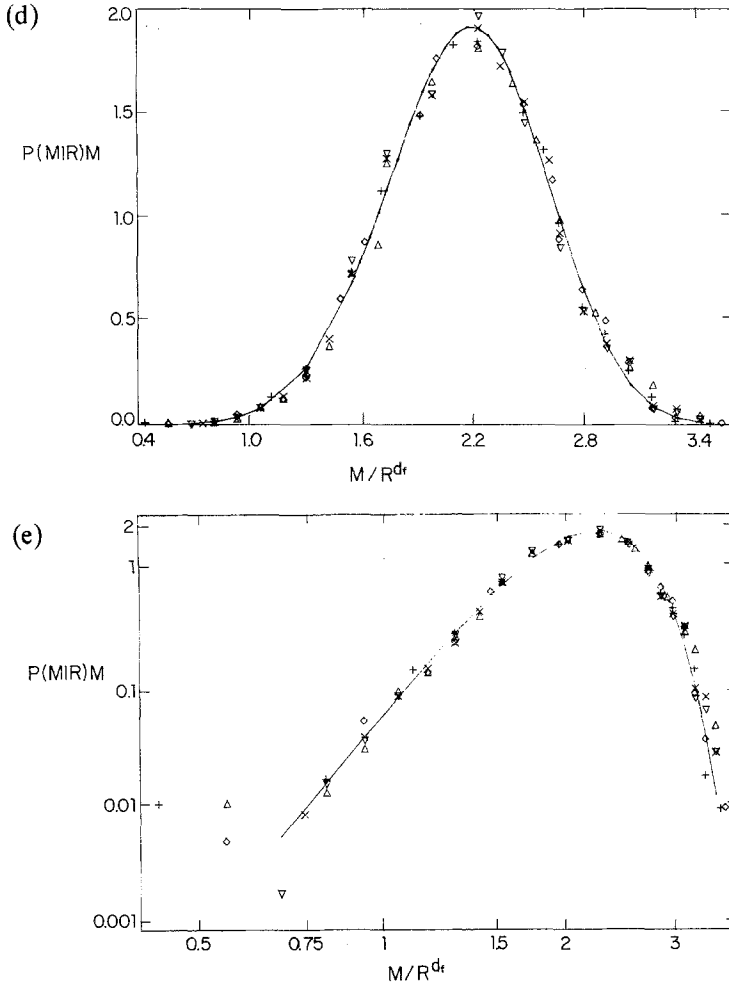[b] Best fit to the form $f_1(X) = \exp(C_1 - A_1 X^{-g_1} - B_1 X^{\delta_1})$.

(a)

P(M|R)M

M / R^{d_f}

(b)

P(M|R)M

M / R^{d_f}

(c)
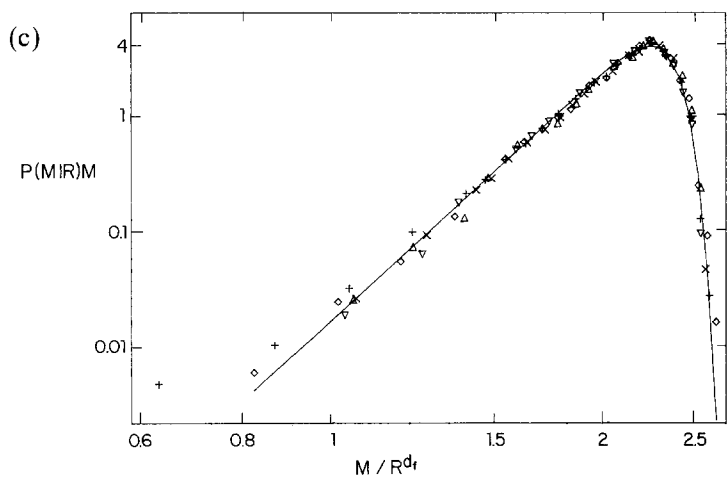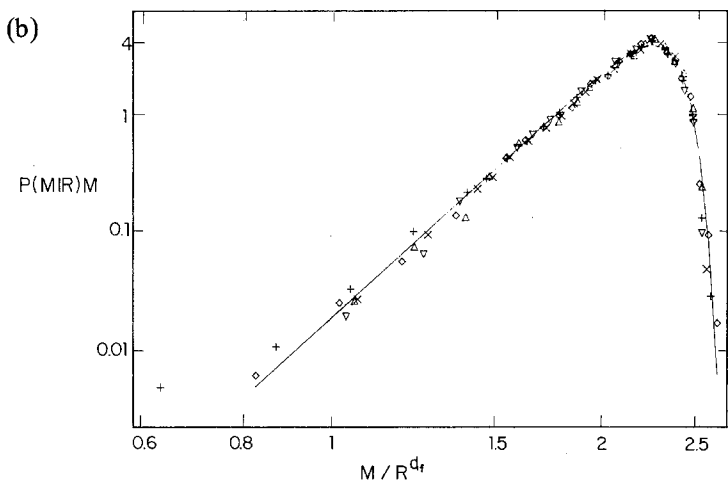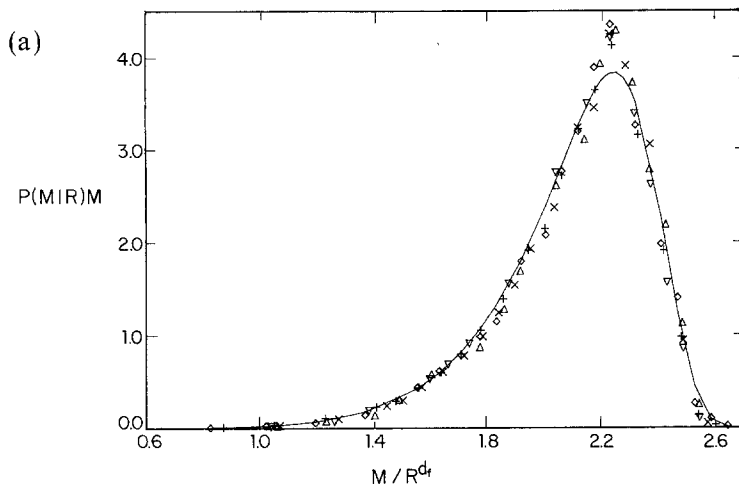
P(M|R)M

M / R^{d_f}

Fig. 7. (a) Plot of $P(M \mid R)M$ versus M/R^{d_f} for $D = 2$ percolation clusters, for different values of R: ($+$) 60 and ($\Diamond$) 100 (for fix $R = 200$) and ($\triangle$) 460, ($\times$) 580, and (∇) 740 (for fix $R = 1000$). The solid line is the theoretical curve, Eq. (4.6), with $\log A_1 = -3.9$, $g_1 = 6.89$, $B_1 = 7 \times 10^{-8}$, and $\delta_1 = 19.1$. (b) Plot of $\log P(M \mid R)M$ versus $\log(M/R^{d_f})$ for the same values of R as in (a). The straight line shown for small M/R^{d_f} suggests a power-exponent form for $f_1(x)$ as in Eq. (4.6). (c) The same as (b), but the solid line represents a theoretical fit to an exponent-exponent function of the form $f_1(x) = C \exp(-Ax^{-g} - Bx^{\delta})$ with $C = 3.2$, $A = 1520$, $g = 0.005$, $B = 6.2 \times 10^{-8}$, and $\delta = 19.2$. (d) Plot of $P(M \mid R)M$ versus M/R^{d_f} for percolation clusters in $D = 3$, for different values of R: ($+$) 24, ($\Diamond$) 26, ($\triangle$) 32, ($\times$) 34, and (∇) 36. The best scaling is achieved with $d_f = 2.50 \pm 0.02$. The solid line represents the best fit with Eq. (4.6) using the parameters $A_1 = 0.06$, $g_1 = 6.3$, $B_1 = 0.055$, and $\delta_1 = 4.2$. (e) Same as (d) on a log-log plot. The scattered data about the straight line below the maximum supports the power-exponent form suggested in Eq. (4.6).

4.2. $P(M|l)$

To study the distribution of mass as a function of the topological distance l, we plot the numerical data for $\log P(M|l)$ versus $\log M$ for several values of l (see Fig. 8a). This figure presents the general form of the probability for having a mass M within a given chemical distance l.

Next we plot $P(M|l)/P(M|l)_{max}$ as function of $M/M_{1/2}$ (Figs. 8b and 8c). One can see that the different curves in Fig. 8a collapse to a single curve in Fig. 8c, indicating the scaling property of $P(M|l)$.

Following the arguments leadings to Eqs. (4.1)–(4.5), we assume a scaling form for the probability density

$$P(M|l) \approx M^{-1} f_2(M/l^{d_l}) \tag{4.7}$$

from which it follows that

$$\langle M^n \rangle = \int M^n M^{-1} f_2(M/l^{d_l}) \, dM \approx l^{nd_l} \tag{4.8}$$

where d_l is the topological fractal dimension. The scaling form of Eq. (4.7) is supported by the straight line whose slope is -1 connecting the maxima $P(M^*|l)$ in Fig. 8a.

To test directly the scaling form suggested in Eq. (4.7), we plot in Figs. 9a and 9c $P(M|l)M$ as a function of M/l^{d_l}. The data collapse shows excellent agreement with the above scaling form. The best scaling is obtained using $d_l = 1.66 \pm 0.01$ in $D = 2$ and $d_l = 1.76 \pm 0.01$ for $D = 3$.

In Figs. 9b and 9d we plot $\log (P(M|l)M)$ as a function of $\log M$ for $D = 2$ and $D = 3$, respectively. Above M^*, $f_2(x)$ falls sharply, suggesting that an exponential form governs this regime. For $M < M^*$, $f_2(x)$ rises rapidly and not linearly, suggesting that an exponential function governs also this regime. Thus, we assume that $f_2(x)$ has an *exp-exp* form,

$$f_2(x) = \exp(C_2 - A_2 x^{-g_2} - B_2 x^{\delta_2}), \qquad x = M/l^{d_l} \tag{4.9}$$

Using best fit techniques for fitting tha data to Eq. (4.9), we obtain numerical values for A_2, B_2, C_2, g_2, and δ_2 given in Table IV. The exp-exp form can be confirmed by calculating from the numerical data

$$z_1 = -\log f_2(x) + C_2 - A_2 x^{-g_2} = B_2 x^{\delta_2} \tag{4.10}$$

and

$$z_2 = -\log f_2(x) + C_2 - B_2 x^{\delta_2} = A_2 x^{-g_2} \tag{4.11}$$

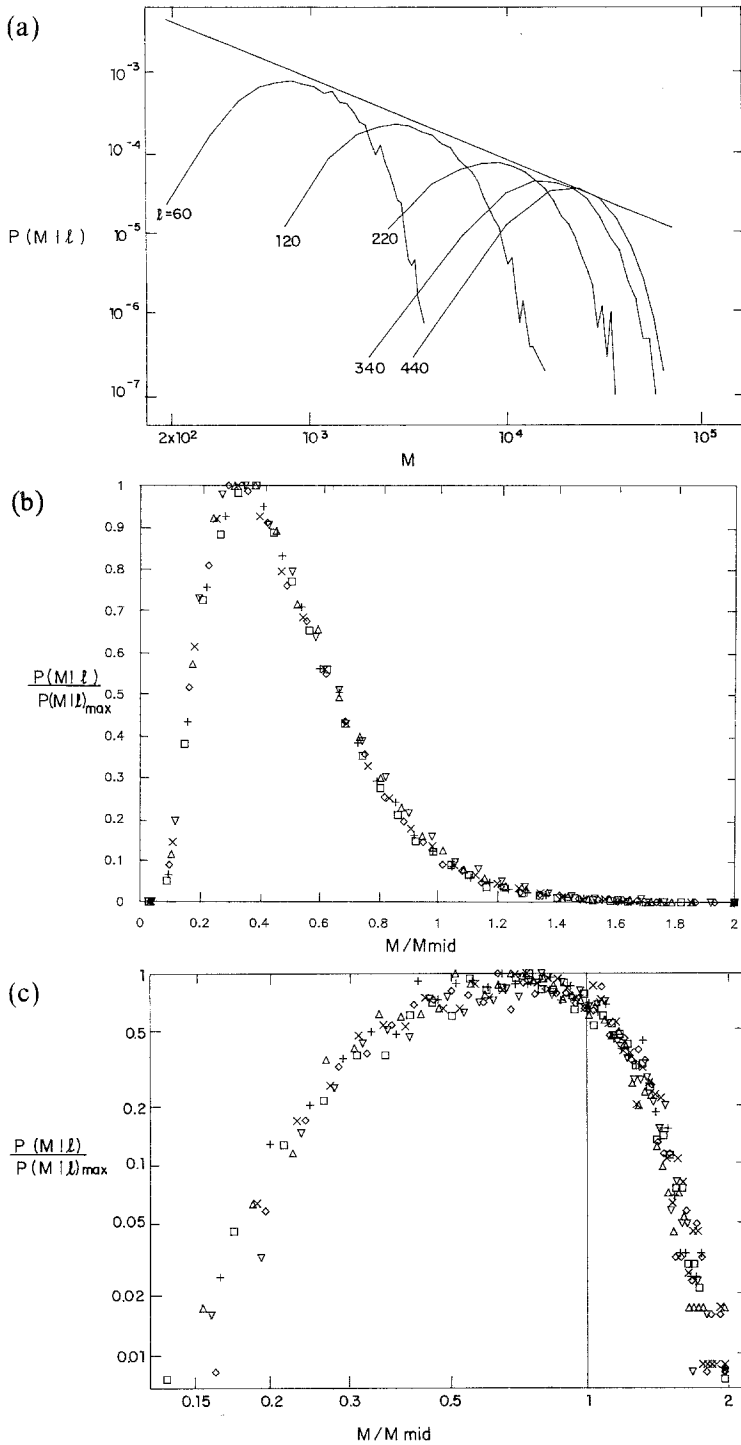Fig. 8. (a) Plot of log $P(M|l)$ versus log M for percolation clusters in $D = 3$ (B.C. min $l = 500$). The slope of the straight line is -1. (b) Plot of $P(M|l)/P(M|l)_{max}$ versus $M/M_{1/2}$ for $D = 3$ (min $l = 200$) for several values of l: ($\square$) 100, ($+$) 120, ($\diamond$) 140, ($\triangle$) 160, ($\times$) 180, ($\triangledown$) 200. The collapse to a single curve indicates the scaling property of $P(M|l)$. (c) Plot of log$\{P(M|l)/P(M|l)_{max}\}$ versus log$\{M/M_{1/2}\}$ for $D = 2$ (min $l = 4000$) for several values of l: ($\square$) 200, ($+$) 600, ($\diamond$) 1200, ($\triangle$) 1600, ($\times$) 2200, ($\triangledown$) 2800.
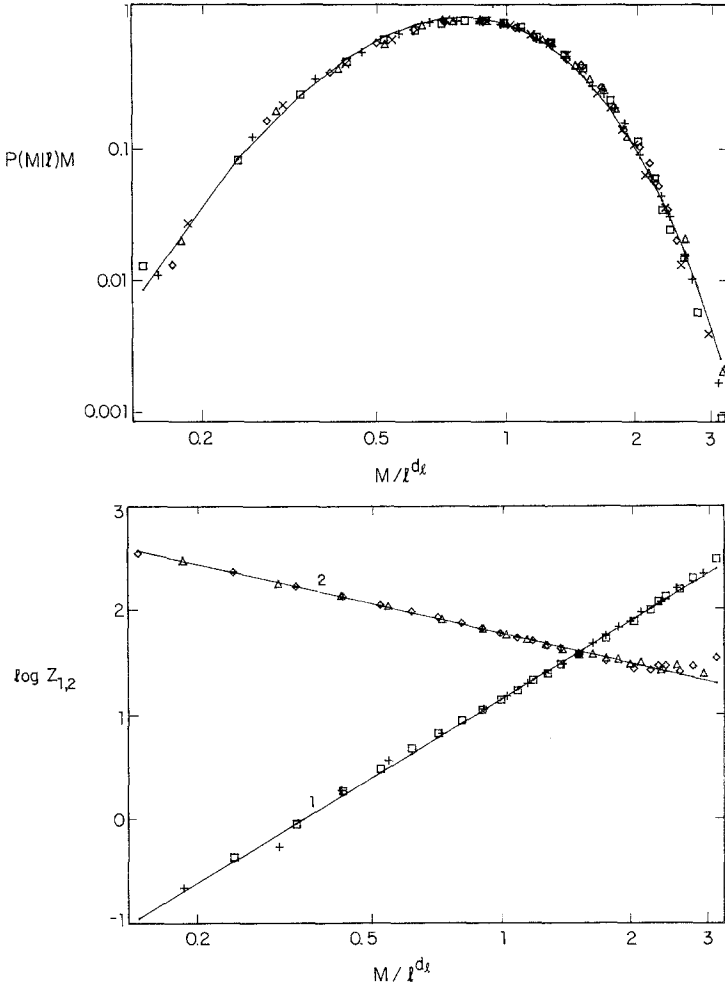
(a)

(b)

(c)
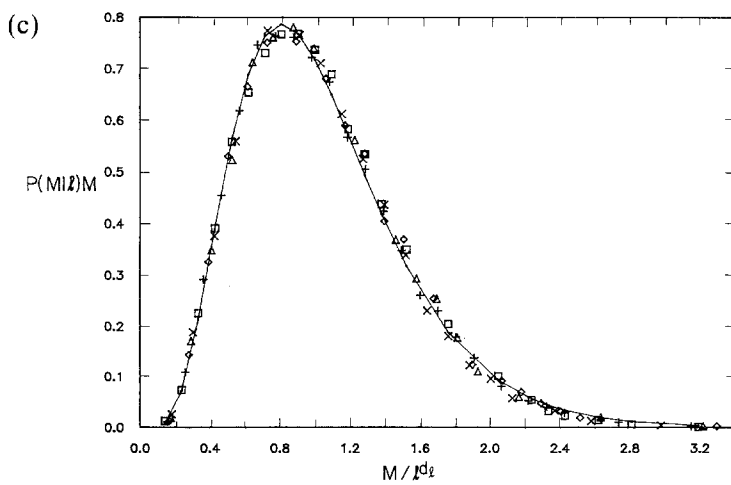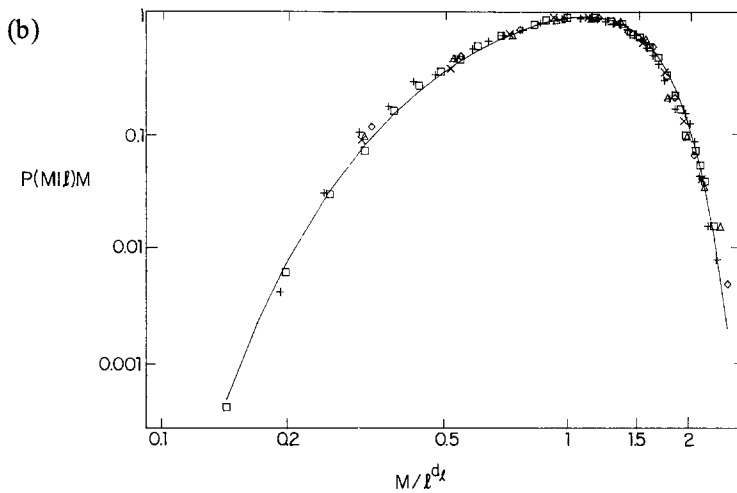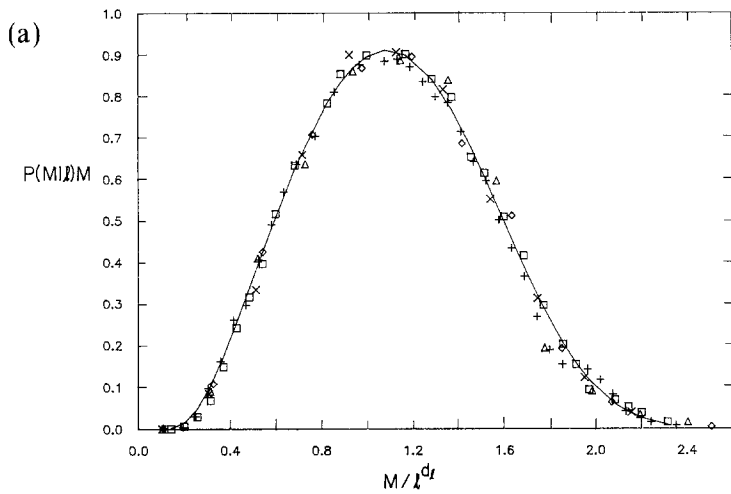
Fig. 9. (a) Plot of $P(M|l)M$ versus M/l^{d_l} for percolation clusters for $D = 2$ and several values of l: ($\square$) 180 and ($+$) 300 (for fix $l = 300$) and ($\diamond$) 600, ($\triangle$) 1200, ($\times$) 1600 (for min $l = 3000$). The data collapse shows excellent agreement with the scaling form, Eq. (4.7). The best scaling is obtained using $d_l = 1.66 \pm 0.01$. The solid curve represents the best fit of Eq. (4.9) to the data using the parameters given in Table IV. (b) The same as (a) on a log-log plot. The curvature seen for $M/l^{d_l} < 1$ indicates that the form of $P(M|l)$ cannot be of a power-exponent type. (c) Plot of $P(M|l)M$ as a function of M/l^{d_l} for percolation clusters for $D = 3$ and several values of l: ($\square$) 70, ($+$) 100 (for min $l = 200$) and ($\diamond$) 140, ($\triangle$) 170, ($\times$) 200 (for min $l = 500$). The best scaling is achieved using $d_l = 1.76 \pm 0.02$. The solid line represents the best fit of Eq. (4.9) to the data using the parameters given in Table IV. (d) The same data as in (c) on a log-log plot. The curvature seen for $M/l^{d_l} < 1$ indicates that the form of $P(M|l)$ is not a power exponent form. (e) Plot of $\log Z_1$ [Eq. (4.10)] and $\log Z_2$ [Eq. (4.11)] as a function of $x = M/l^{d_l}$. The data fit in general to straight lines, supporting Eq. (4.9).

Table IV.   The Parameters Obtained from a Best Fit to the
Scaling Form of $P(M|l)^a$

	$D = 2$	$D = 3$	$D = 6^b$
d_l	1.66 ± 0.01	1.76 ± 0.01	2
C_2	1.13 ± 0.01	8.78 ± 0.02	—
A_2	1.07 ± 0.02	5.94 ± 0.02	—
g_2	1.00 ± 0.05	0.41 ± 0.01	1
B_2	0.165 ± 0.005	3.16 ± 0.02	—
δ_2	4.10 ± 0.05	1.09 ± 0.03	1

^{a} Eq. (4.9), $f_2(X) = \exp(C_2 - A_2 X^{-g_2} - B_2 X^{\delta_2})$.
^{b} For percolation on a Cayley tree.[32]

If Eq. (4.9) is valid, we expect that $\log z_1$ and $\log z_2$ versus $\log x$ would yield straight lines. Indeed, two straight lines with the appropriate slopes δ_2 and $-g_2$ are seen in Fig. 9e.

4.3. $P(R|l)$

The distribution of the geometrical distance R between two sites as a function of their topological distance l is presented in Fig. 10a. We plot the numerical data for $\log P(R|l)$ versus $\log R$ for several values of l.

Next we plot $P(R|l)/P(R|l)_{\max}$ as a function of $R/R_{1/2}$; examples are shown in Figs. 10b and 10c. The different curves in Fig. 10a collapse to one curve in Fig. 10c, indicating the scaling property of $P(R|l)$.

Following the arguments leading to Eqs. (4.1)–(4.5), we assume (see also ref. 34) a scaling form for the probability density

$$P(R|l) \approx R^{-1} f_3(R/l^{\tilde{\nu}}) \tag{4.12}$$

from which it follows that

$$\langle R^n \rangle = \int R^n R^{-1} f_3(R/l^{\tilde{\nu}}) \, dR \approx l^{n\tilde{\nu}} \tag{4.13}$$

where $\tilde{\nu}$ is the exponent relating intrinsic and extrinsic distances. The scaling form of Eq. (4.12) is supported by the straight line whose slope is -1 connecting the maximas $P(R^*|l)$ in Fig. 10a.

To test directly the scaling form suggested in Eq. (4.12), we plot in Figs. 11a and 11c $P(R|l)R$ as a function of $R/l^{\tilde{\nu}}$. The data collapse shows
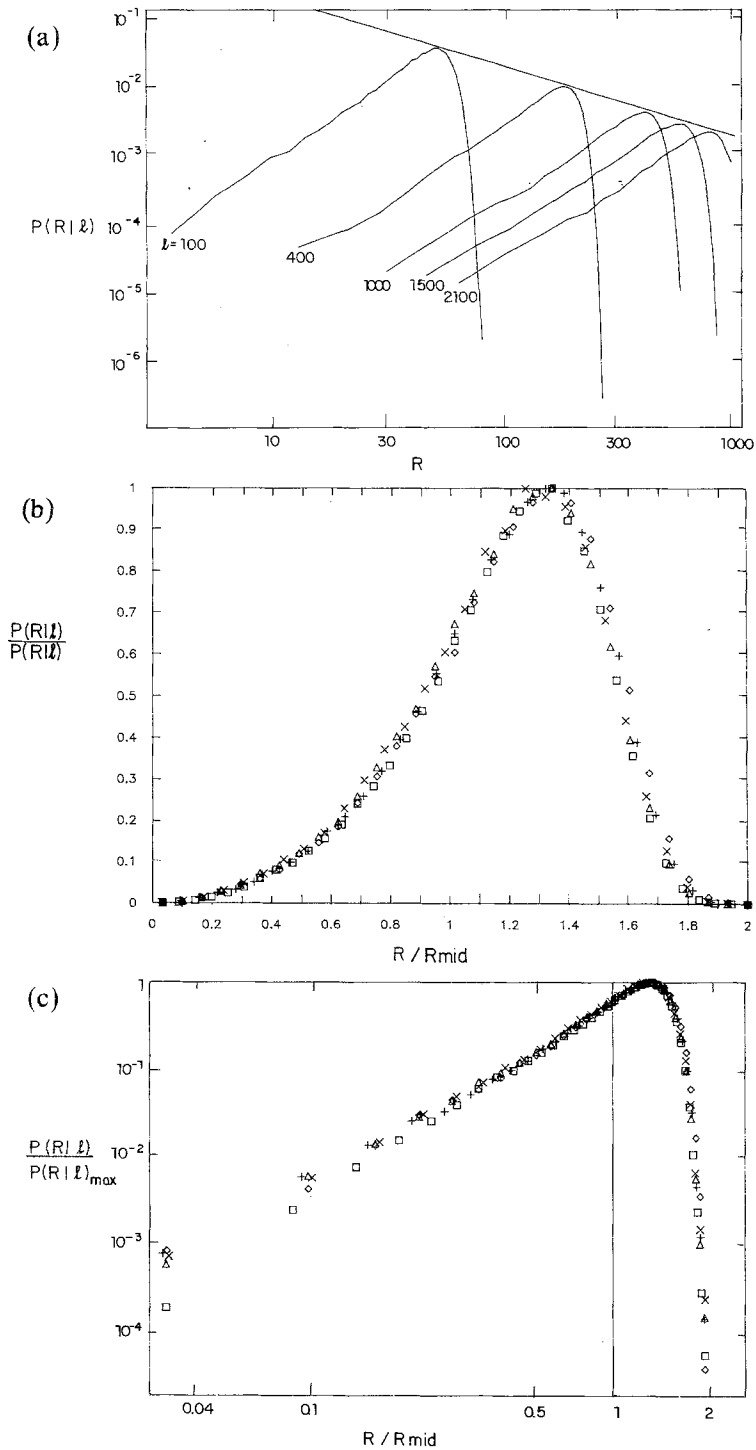
Fig. 10. (a) Plot of log $P(R|l)$, the distribution of the geometrical distance R, for a given chemical distance l for $D = 2$ and min $l = 4000$. The straight line (whose slope is -1) supports the scaling form of Eq. (4.12). (b) Plot of $P(R|l)/P(R|l)_{max}$ as a function of $R/R_{1/2}$ for the data shown in (a). Note the data collapse of the different values of l: ($\square$) 200, ($+$) 600, ($\diamond$) 1000, ($\triangle$) 1200, and ($\times$) 1600. (c) Plot of log$\{P(R|l)/P(R|l)_{max}\}$ as a function of log $R/R_{1/2}$ for the data presented in (b).
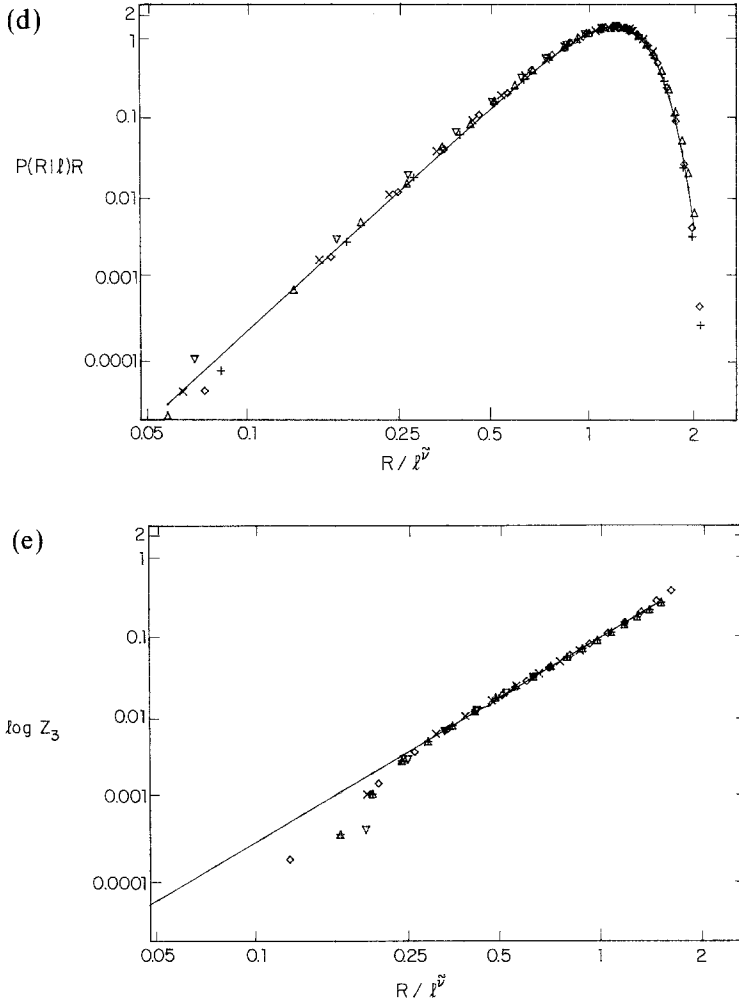
(a)

(b)

(c)

(d)

(e)
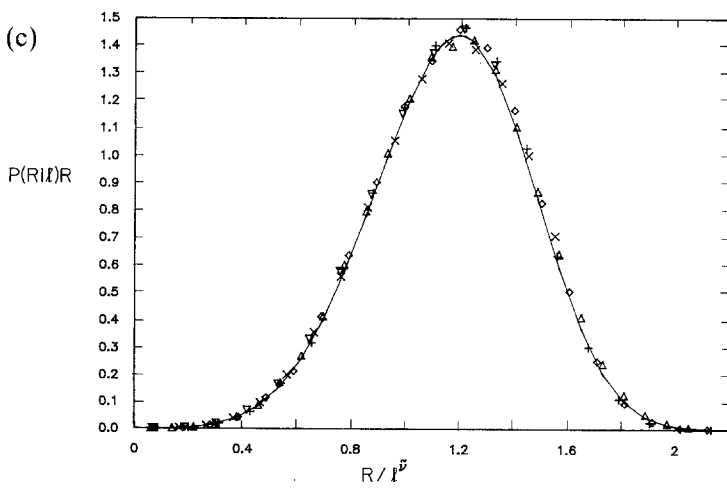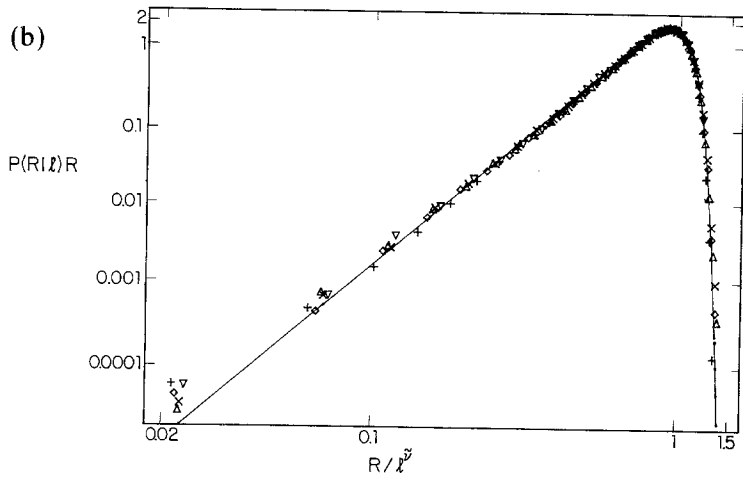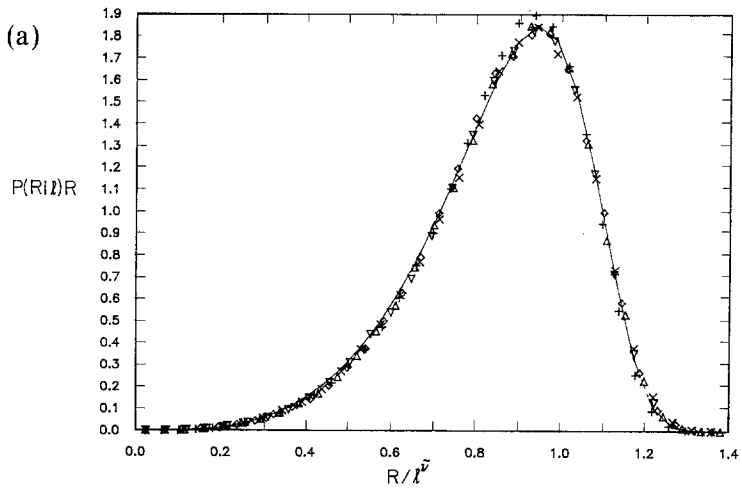
Fig. 11.   (a) Plot of $P(R|l)R$ as a function of $R/l^{\tilde{\nu}}$ for the data shown in Fig. 10. The solid curve represents the best fit of Eq. (4.14) to the data, obtained using the parameters given in Table V. (b) Plot of log $(P(R|l)R)$ as a function of log $R/l^{\tilde{\nu}}$. The solid line represents a fit to Eq. (4.14) with $A_3 = 3.00 \pm 0.05$, $g_3 = 3.25 \pm 0.05$, $B_3 = 0.54 \pm 0.04$, and $\delta_3 = 9.8 \pm 0.2$. The straight line to the left of the maximum supports the power-exponent form suggested for $P(R|l)$. Note, however, the slight deviation from the straight line for very small values of $R/l^{\tilde{\nu}}$. (c) Plot of $P(R|l)R$ versus $R/l^{\tilde{\nu}}$ for percolation clusters for $D = 3$ for several values of l: ($+$) 60, ($\diamond$) 70, ($\triangle$) 100, ($\times$) 130, and ($\triangledown$) 160 (for min $l = 200$). The best scaling was achieved using $\tilde{\nu} = 0.70 \pm 0.01$. The solid curve represents the best fit of Eq. (4.14) to the data using the parameter given in Table V. (d) The same data as in (c) on a log-log plot. The straight line for $R/l^{\tilde{\nu}} < 1$ supports the power-exponent form for $P(R|l)$ also for $D = 3$. (e) Plot of log Z_3, Eq. (4.15), versus $x = R/l^{\tilde{\nu}}$ for $D = 3$. The range of the straight line is the range where the power-exponent form is valid.

Table V.   The Parameters Obtained from a Best Fit to the
Scaling Form of $P(R|l)^a$

	$D = 2$	$D = 3$	$D = 6^b$
$\tilde{v}$	0.875 ± 0.005	0.70 ± 0.01	0.5
A_3	3.00 ± 0.05	1.82 ± 0.05	—
g_3	3.25 ± 0.05	3.98 ± 0.05	—
B_3	0.54 ± 0.04	0.43 ± 0.01	—
δ_3	9.8 ± 0.2	4.21 ± 0.03	2

^{a} Eq. (4.14), $f_3(X) = A_3 X^{g_3} \exp(-B_3 X^{\delta_3})$, $X = R/l^{\tilde{v}}$.
^{b} Cayley tree results.[32]

excellent agreement with the above scaling form. The best scaling is obtained using $\tilde{v} = 0.875 \pm 0.005$ for $D = 2$ and $\tilde{v} = 0.700 \pm 0.005$ for $D = 3$.

In Figs. 11b and 11d we plot $\log (P(R|l)R)$ as a function of $\log R$ for $D = 2$ and $D = 3$, respectively. Above R^*, $f_3(x)$ falls sharply, suggesting that an exponential form governs this regime. On the other hand, for $R < R^*$, $\log f_3(x)$ rises linearly, suggesting that a power law governs this regime. Thus, we assume that $f_3(x)$ has an *power-exp* form,

$$f_3(x) = A_3 x^{g_3} \exp(-B_3 x^{\delta_3}), \qquad x = R/l^{\tilde{v}} \tag{4.14}$$

Using best fit techniques for fitting the data to Eq. (4.14), we obtain numerical values for A_3, B_3, g_3, and δ_s given in Table V. The power law in Eq. (4.14) is seen easily in Figs. 11b and 11d; however, to confirm the exponential regime in Eq. (4.14) we calculate from the numerical data

$$z_3 = -\log f_3(x) + \log A_3 + g_3 \log x = B_3 x^{\delta_3} \tag{4.15}$$

Ploting $\log z_3$ versus $\log x$ should give a straight line, which is seen in the exponential regime in Fig. 11e.

5. DISCUSSION AND CONCLUSIONS

The exponents d_f, d_l, and $\tilde{v}$ calculated independently in this work are related by[9]

$$\tilde{v} = d_l/d_f \tag{5.1}$$

The numerical values for d_f, d_l, and $\tilde{v}$ found for two and three dimensions (see Table VI) are indeed in exellent agreement with Eq. (5.1).

Table VI. The Critical Exponents for the Structural Properties of Percolation Clusters

D	d_f	d_l	$\tilde{\nu}$
2	1.896	1.66 ± 0.01	0.875 ± 0.005
3	2.50 ± 0.02	1.76 ± 0.01	0.70 ± 0.01
6	4	2	0.5

Generally our numerical data suggest that the various moments of $M(R)$, $M(l)$, and $R(l)$ can be represented as a power of their first moment, indicating that all moments (positive and negative) are determined by a single gap exponent (see Figs. 1a, 1b, 2a, 2b, 3a, and 3b).

It should be noted that although the structural distributions of percolation do not seem to be of multifractal nature, diffusion on such structure might have multifractal features.[35]

A relation between the exponents δ_3 and $\tilde{\nu}$, characterizing $P(R \mid l)$, was suggested in ref. 34,

$$\delta_3 = (1 - \tilde{\nu})^{-1} \qquad (5.2)$$

The numerical values for $\tilde{\nu}$ and δ_3 obtained in the present work are not consistent with the above relation for both $D = 2$ and 3 (see Tables V and VI). A possible explanation for the disagreement is as follows. Relation (5.2) is derived[20,34] from the expression of the enlongation,

$$\langle r \rangle \approx \int \exp(\beta f r) \exp(-r/N^{\tilde{\nu}})^{\delta_3} \, dr \qquad (5.3)$$

and by the assumption that $r \approx N^\varepsilon$ with $\varepsilon = 1$. This might be true for SAWs on structures without holes (such as Euclidean lattices) or loopless structures for which by definition holes do not exist, but in the case of percolation in $D = 2$ or 3 we suspect that $\varepsilon < 1$. Thus Eq. (5.2) is modified to be

$$\delta_3 = (1 - \tilde{\nu}/\varepsilon)^{-1} \qquad (5.4)$$

which predicts a larger value for δ_3. Using the numerical values for δ_3 obtained in this work, we find that $\varepsilon = 0.975 \pm 0.005$ for $D = 2$ and $\varepsilon = 0.92 \pm 0.01$ for $D = 3$. Thus, the question about the existence of a relation between $\tilde{\nu}$ and δ_3 is still open.

The density distributions $P(M|R)$, $P(M|l)$, and $P(R|l)$ are related through the convolution integral,

$$P(M|l) = \int P(M|R) \, P(R|l) \, dR \tag{5.5}$$

Substituting the forms suggested for $P(M|R)$, $P(M|l)$, and $P(R|l)$ by Eqs. (4.6), (4.9), and (4.14), respectively, and using the steepest descent method, one obtains a relation for δ_1, δ_2, and δ_3:

$$\delta_2 = \delta_1 \delta_3 / (\delta_1 d_f + \delta_3) \tag{5.6}$$

Indeed, the numerical values obtained for the above exponents are in very good agreement with Eq. (5.6) (see Tables III–VI).

The functional form of $f_i(x)$ for large x seems to be of the form $\exp(-B_i x^{\delta_i})$ for all cases. However, the form of $f_i(x)$ for small x ($x < x^*$) is not yet clear. On one hand, the form of $P(R|l)$ in this regime seems to be dominated by a power law x^{g_3}, as seen in Figs. 11b and 11d. On the other hand, $P(M|l)$ cannot be explained by a power function in the small-x regime (see Figs. 9b and 9d), but only by an exponential. As for $P(M|R)$, if we assume that for $x < x^*$, $f_1(x)$ has a power law behavior, then the convolution integral in Eq. (5.5) could not be solved for the lower regime of x, since an integral of two power laws cannot yield an exponential. Thus, we assume that also $f_1(x)$ has an exponential form $\exp(-x^{-g_1})$ for $x < 1$. Using best fit techniques, we obtain a small value for g_1; see Table III and Fig. 7c. Thus we conjecture that both $P(M|R)$ and $P(M|l)$ have an exp-exp form and $P(R|l)$ has a power-exp form. This can be explained by the fact that the mass within a radius R or a chemical distance l must have a minimal cutoff value, but the radius R can be very small even for very large chemical distances.

It is interesting to compare our results to those obtained for percolation clusters generated on a Cayley tree at criticality.[32] Analytical calculations show that $P(M|l)$ is of the form

$$P(M|l) = A/\langle M \rangle \exp(-ax^{g_2} - bx^{\delta_2}), \qquad x = M/l^2 \tag{5.7}$$

where $g_2 = \delta_2 = 1$. This form supports our suggestion that the form of $P(M|l)$ for $D = 2$ and $D = 3$ consists of two exponentials; see Eq. (4.9). From Eq. (5.7) it also follows that $\langle M \rangle \approx l^2$ and $d_l = 2$ for $D = 6$. Since every path on the Cayley tree is a random walk (when embedded in $D = \infty$), $P(R|l)$ is dominated for $R^2/l > 1$ by $\exp(-R^2/l)$. Thus, $\delta = 2$ for $D = 6$, and since $R^2 \approx l$, it follows that $\tilde{\nu} = 0.5$ for $D = 6$. These results are summarized for comparison with those for other dimensions in Tables III–VI.

Several types of cluster aggregates have also been studied recently[31] using a similar approach. For the screen growth model and for the cluster–cluster aggregates, $P(M \mid R)$ was studied and found to scale as

$$P(M \mid R) \approx M^{-1} f(M/R^{d_f}) \tag{5.8}$$

However, the form of $f(x)$ in this case seems to have three regimes of different behaviors. For $x \ll 1$, $f(x)$ behaves as $\exp(-x^{-\gamma})$; for $x \approx 1$ a power law behavior is seen, $f(x) \approx x^g$; and for $x \gg 1$ an exponential decay $f(x) \approx \exp(-x^\delta)$. The DLA seems to have a more complicated structure, since it cannot be explained[31] by the above scaling form suggested for $P(M \mid R)$, and the moments cannot be explained by a single gap exponent.

ACKNOWLEDGMENTS

REFERENCES

1. P. L. Leath, *Phys. Rev. B* **14**:5046 (1976).
2. H. E. Stanley, *J. Phys. A* **10**:L211 (1977).
3. S. Kirkpatrick, in *Inhomogeneous Superconductors*, D. U. Gubser, T. L. Francarilla, J. R. Leibowitz, and S. A. Wolf (AIP Conference Proceedings 58, American Institute of Physics, New York, 1979).
4. D. Stauffer, *Introduction to Percolation Theory* (Taylor and Francis, London, 1985).
5. Z. Alexandrowicz, *Phys. Lett.* **80A**:284 (1980).
6. R. Pike and H. E. Stanley, *J. Phys. A* **14**:L169 (1981).
7. B. B. Mandelbrot, *Fractals: Form, Chance and Dimension* (Freeman, San Francisco, 1977); *The Fractal Geometry of Nature* (Freeman, San Francisco, 1982).
8. P. Grassberger, *Math. Biosci* **62**:157 (1983); *J. Phys. A* **19**:1681 (1986); *J. Phys. A* **18**:L215 (1985).
9. S. Havlin and R. Nossal, *J. Phys. A* **17**:L427 (1984).
10. G. Deutscher, R. Zallen, and J. Adler (eds.), *Percolation Structures Processes* (Hilgen, Bristol, 1983).
11. A. Aharony, in *Directions in Condensed Matter Physics*, G. Grinstein and G. Mazenko, eds. (World Scientific, Singapore, 1986).
12. A. Coniglio, *J. Phys. A* **15**:3829 (1982).
13. S. Havlin and D. Ben-Avraham, *Adv. Phys.* **36**:695 (1987).
14. H. E. Stanley, *J. Stat. Phys.* **36**:843 (1984).
15. A. Bunde, *Adv. Solid State Phys.* **26**:113 (1986).
16. R. Pynn and A. Skjeltorp (eds.), *Scaling Phenomena in Disordered Systems* (Plenum Press, New York, 1985).
17. H. J. Herrmann, *Phys. Rep.* **136**:153 (1986).

18. F. Family and D. P. Landau (eds.), *Proceedings International Topical Conference Kinetics of Aggregation and Felation* (North-Holland, Amsterdam, 1984).
19. H. E. Stanley and N. Ostrowsky (eds.), *On Growth and Form* (Nijhoff, Boston, 1986).
20. P. G. de Gennes, *Scaling Concepts in Polymer Physics* (Cornell University Press, Ithaca, New York, 1979).
21. L. Pietronero and E. Tosatti (eds.), *Fractals in Physics* (North-Holland, Amsterdam, 1986).
22. H. E. Stanley, *Introduction to Fractal Phenomena* (1987).
23. D. Stauffer, *Z. Phys.* **37**:89 (1980).
24. L. de Arcangelis, S. Redner, and A. Coniglio, *Phys. Rev. B* **31**:4725 (1985); **34**:4656 (1986).
25. P. Meakin, H. E. Stanley, A. Coniglio, and T. A. Witten, *Phys. Rev. A* **32**:2364 (1985); P. Meakin, A. Coniglio, H. E. Stanley, and T. A. Witten, *Phys. Rev. A* **34**:3325 (1986).
26. T. L. Halsey, P. Meakin, and I. Procaccia, *Phys. Rev. Lett.* **56**:854 (1986).
27. C. Amitrano, A. Coniglio, and F. di Liberto, *Phys. Rev. Lett.* **57**:1016 (1986).
28. B. B. Mandelbrot, in *Proceeding of the 13th IUPAP Conference on Statistical Physics*, E. Cabib, C. G. Kuper, and I. Reiss, eds. (Hilger, Bristol, 1978).
29. T. C. Halsey, M. H. Jensen, L. P. Kadanoff, I. Procaccia, and B. I. Shraiman, *Phys. Rev. A* **33**:1141 (1986).
30. H. G. E. Hentschel and I. Procaccia, *Physica D* **8**:435 (1983).
31. P. Meakin and S. Havlin, *Phys. Rev. A* **36**:4428 (1987).
32. S. Havlin, J. Kiefer, F. Leyvraz, and G. H. Weiss, *J. Stat. Phys.* **47**:173 (1987).
33. W. C. Hamilton, *Statistics in Physical Science* (Ronald Press, New York, 1964).
34. S. Havlin, B. L. Trus, G. H. Weiss, and D. Ben-Avraham, *J. Phys. A* **18**:L247 (1985).
35. S. Havlin and O. Matan, *J. Phys. A* **21**:L307 (1988).